

See discussions, stats, and author profiles for this publication at: <https://www.researchgate.net/publication/334559883>

Performance of a 3D pendulum tuned mass damper in offshore wind turbines under multiple hazards and system variations

Article in Smart Structures and Systems · July 2019

DOI: 10.12989/sss.2019.24.1.053

CITATIONS

0

READS

318

3 authors, including:



Vahid Jahangiri

Louisiana State University

10 PUBLICATIONS 64 CITATIONS

[SEE PROFILE](#)



Chao Sun

Louisiana State University

27 PUBLICATIONS 268 CITATIONS

[SEE PROFILE](#)

Some of the authors of this publication are also working on these related projects:



Vibration Control of Monopile Offshore Wind Turbine [View project](#)



Concrete Constitutive Law Modeling Using CT Technique [View project](#)

Performance of a 3D Pendulum Tuned Mass Damper in Offshore Wind Turbines under Multiple Hazards and System Variations

Chao Sun^{*1}, Vahid Jahangiri¹, Hui Sun²

¹ Department of Civil and Environmental Engineering, Louisiana State University, Baton Rouge 70803, USA

² Xi'an Research Institute Co., Ltd. of China Coal Technology & Engineering Group, Xi'an, 710077, China

Abstract

Misaligned wind-wave and seismic loading render offshore wind turbines suffering from excessive bi-directional vibration. However, most of existing research in this field focused on unidirectional vibration mitigation, which is insufficient for research and real application. Based on the authors' work (C. Sun and Jahangiri 2018), the present study uses a three dimensional pendulum tuned mass damper (3d-PTMD) to mitigate the nacelle structural response in the fore-aft and side-side directions under wind, wave and near-fault ground motions. An analytical model of the offshore wind turbine coupled with the 3d-PTMD is established wherein the interaction between the blades and the tower is modelled. Aerodynamic loading is computed using the Blade Element Momentum (BEM) method where the Prandtl's tip loss factor and the Glauert correction are considered. Wave loading is computed using Morison equation in collaboration with the strip theory. Performance of the 3d-PTMD is examined on a National Renewable Energy Lab (NREL) monopile 5 MW baseline wind turbine under misaligned wind-wave and near-fault ground motions. The robustness of the mitigation performance of the 3d-PTMD under system variations is studied. Dual linear TMDs are used for comparison. Research results show that the 3d-PTMD responds more rapidly and provides better mitigation of the bi-directional response caused by misaligned wind, wave and near-fault ground motions. Under system variations, the 3d-PTMD is found to be more robust than the dual linear TMDs to overcome the detuning effect. Moreover, the 3d-PTMD with a mass ratio of 2% can mitigate the short-term fatigue damage of the offshore wind turbine tower by up to 90%.

Keywords: Offshore wind turbines; bi-directional response mitigation; wind-wave misalignment; three dimensional pendulum damper; near-fault seismic protection; fatigue damage mitigation

1. Introduction

Increasing demand for renewable energy has led to a significant growth in wind energy production. Offshore wind turbines (OWTs) have been more attractive than their onshore counterparts due to steadier and higher wind speeds, fewer space limitations, lower visual impact and less noise pollutions in the marine area. However, because of the severe marine conditions such as strong wind, wave and storm surge, the OWTs always suffer from excessive vibrations which will compromise the power output and cause fatigue damage or even collapse.

To mitigate the vibration of the OWTs, numerous controlling methods have been studied. Colwell and Basu (2009) used the tuned liquid column damper to control the vibration of the OWT. It was found that the tuned liquid column damper could increase the tower fatigue life. Zuo et al. (2017) proposed using multiple tuned mass dampers to control the tower vibrations of a monopile OWT. Also, the authors studied the robustness of the multiple TMDs by assuming some dampers lose their functionality. Passive structural control strategies may lose their effectiveness in the presence of system and environmental variations. Hence, researchers have focused on active or

^{*}Corresponding author, Assistant professor, E-mail: csun@lsu.edu

semi-active control strategies. Fitzgerald et al. (2018) proposed a novel blade pitch control strategy to reduce the vibrations of the blade. The authors concluded that the proposed controller is capable of reducing the out-plane blade vibrations significantly. Sun (2018a, b) introduced a semi-active TMD (STMD) with tunable natural frequency and damping ratio which utilizes short Fourier transform control algorithm to mitigate the monopile OWT vibrations. It was found that with damage presence in the foundation and tower, the passive TMD loses part of its effectiveness while the STMD remains effective successfully in mitigating the structural response. Dinh et al. (2016) used an STMD placed in the spar floating wind turbine blades, nacelle and platform. It was observed that the STMD is more effective than the passive TMD when subjected to time-variant rotor speed, blade stiffness and mooring cable tension. Arrigan et al. (2014) studied the effectiveness of an STMD in mitigating the edgewise vibrations of wind turbine blades. The effectiveness of the STMD was evaluated under different loading and operational conditions.

While most of current research focus on mitigating the vibration primarily in the fore-aft direction, OWTs always suffer from bi-directional vibrations due to vortex induced vibrations (VIVs) and wind-wave misalignment. Stewart and Lackner (2014) used dual linear TMDs to mitigate the bi-directional vibration and found that the dual TMDs could mitigate the fore-aft and side-side fatigue load. However, several drawbacks such as a larger TMD mass, space, and higher cost of installation exist when using linear dual TMDs. In this regard, based on one of coauthor's previous work (C Sun, Nagarajaiah, and Dick 2014a; C. Sun, Nagarajaiah, and Dick 2014b) on planar pendulum mass damper, Sun and Jahangiri (2018; 2019) introduced a passive three dimensional pendulum TMD to control the bi-directional vibrations of a monopile OWT. The authors found that the proposed 3d-PTMD is more effective than the dual linear TMDs. However, the performance of the 3d-PTMD under near-fault ground motions, which is more hazardous to structures, and system variations is not examined in Sun and Jahangiri (2018; 2019)

Therefore, the present paper further examines the performance of the three-dimensional PTMD (3d-PTMD) in mitigating the bi-directional responses under misaligned wind, wave and near-fault ground motions. System variations represented by tower and foundation damage is also considered. A fully coupled nonlinear mathematical model of the monopile OWT coupled with the 3d-PTMD is established. The performance of the 3d-PTMD in mitigating the vibration in fore-aft and side-side directions is evaluated and compared with dual linear TMDs under misaligned wind-wave and near-fault ground motions. The robustness of mitigation performance of the proposed 3d-PTMD is evaluated under different tower and foundation damage cases. In addition, rain flow counting method is used to examine the effectiveness of the 3d-PTMD in mitigating the fatigue damage of the wind turbine tower. Results show that the 3d-PTMD outperforms linear dual TMDs in controlling the bi-directional vibrations of the OWT in the presence of system variations and under misaligned wind-wave and near-fault ground motions. It is found that the 3d-PTMD with a mass ratio of 2% can mitigate the short-term fatigue damage of the offshore wind turbine tower by 90%. In addition, the 3d-PTMD undergoes a smaller stroke than the linear TMDs, which is valuable for practical application considering the limited space in the nacelle.

2. Establishment of the analytical model

A fully coupled three dimensional dynamic model for a monopile OWT with a 3d-PTMD is established using Euler-Lagrangian equation. Fig. 1 illustrates the schematic model of the OWT with a 3d-PTMD placed in the nacelle. The controlled offshore wind turbine system contains 14 degrees of freedom (DOF). The blade in-plane and out-plane coordinates are denoted as $q_1 \sim q_6$;

The nacelle fore-aft and side-side coordinate are denoted as $q_7 \sim q_8$; the foundation translational and rotational coordinates are denoted as $q_9 \sim q_{12}$; The relative coordinate of the 3d-PTMD with respect to the wind turbine nacelle is denoted as $q_{13} \sim q_{14}$.

In Fig. 1(a), wind-wave misalignment is considered and denoted as β and wind-earthquake misalignment is denoted by β_2 . As illustrated in Fig.1 (c) and (d), two linear viscous dampers are attached to the pendulum with damping coefficients of c_{px} and c_{py} , in x_r and y_r directions.

The Euler-Lagrangian equation is used to establish the EOMs of the monopile OWT coupled with 3d-PTMD.

$$\frac{d}{dt} \frac{\partial T(t, \tilde{q}(t), \dot{\tilde{q}}(t))}{\partial \dot{q}_i(t)} - \frac{\partial T(t, \tilde{q}(t), \dot{\tilde{q}}(t))}{\partial q_i(t)} + \frac{\partial V(t, \tilde{q}(t))}{\partial q_i(t)} = Q_i(t) \quad (1)$$

where T and V are the kinetic and potential energy, $\tilde{q}(t)$ is the generalized coordinates vector, $Q_i(t)$ is the generalized force corresponding to the i^{th} component of $\tilde{q}(t)$.

The absolute displacement of the nacelle in the fore-aft direction u_{nac}^{fa} and the side-side direction u_{nac}^{ss} can be expressed as:

$$u_{nac}^{fa} = q_7 + q_9 + h \tan(q_{10}) \approx q_7 + q_9 + h q_{10}, \quad u_{nac}^{ss} = q_8 + q_{11} + h \tan(q_{12}) \approx q_8 + q_{11} + h q_{12} \quad (2)$$

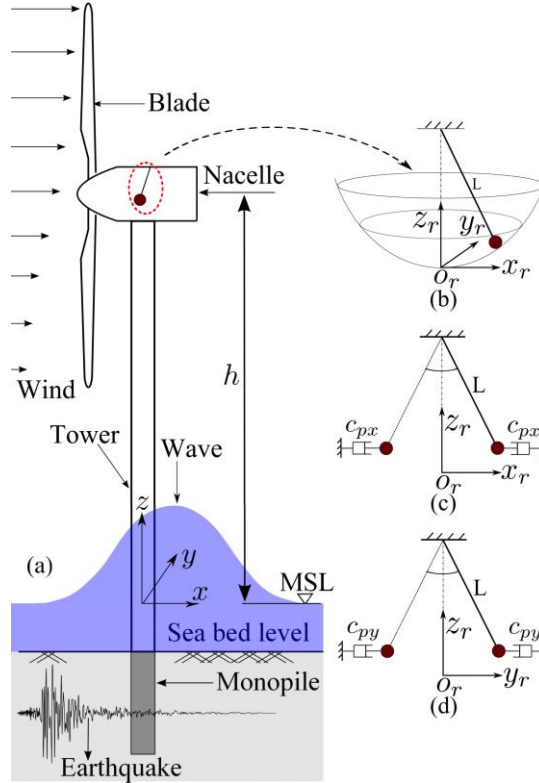


Fig. 1 Monopile OWT coupled with a 3d-PTMD under wind, wave and seismic loading. (a) original schematic model; (b) configuration of the pendulum damper; (c) pendulum model in xz plane; (d) pendulum model in yz plane.

According to Fig.1, the absolute coordinate of the pendulum can be defined as:

$$x_p = u_{nac}^{ss} + x_r, \quad y_p = u_{nac}^{fa} + y_r, \quad z_p = L - \sqrt{L^2 - x_r^2 - y_r^2} \quad (3)$$

The kinetic energy of the pendulum is determined as follows:

$$\begin{aligned} T_p &= \frac{1}{2} m_p [\dot{x}_p^2 + \dot{y}_p^2 + \dot{z}_p^2] \\ &= \frac{1}{2} m_p \left[(v_{nac}^{ss})^2 + (v_{nac}^{fa})^2 + 2v_{nac}^{ss} \dot{x}_r + 2v_{nac}^{fa} \dot{y}_r + \dot{x}_r^2 + \dot{y}_r^2 + \frac{(x_r \dot{x}_r + y_r \dot{y}_r)^2}{L^2 - x_r^2 - y_r^2} \right] \end{aligned} \quad (4)$$

where m_p is the pendulum mass, v_{nac}^{ss} and v_{nac}^{fa} are the absolute velocity of the nacelle in side-side and fore-aft directions.

Due to space limitation, the motion of the blade and the absolute velocity of the tower are not presented here and the equations can be found in (C. Sun 2018a).

The kinetic energy of the wind turbine system with coupled 3d-PTMD can be expressed as:

$$T = \frac{1}{2} \sum_{j=1}^3 \int_0^R \bar{m} v_{bj}^2(r, t) dr + \frac{1}{2} M_{nac} v_{nac}^2 + \frac{1}{2} \int_0^h \bar{M} v_{tow}^2 dz + \frac{1}{2} M_f [\dot{q}_9^2(t) + \dot{q}_{11}^2(t)] + \frac{1}{2} I_f [\dot{q}_{10}^2(t) + \dot{q}_{12}^2(t)] + T_p \quad (5)$$

where M_{nac} is the mass of the nacelle including the hub, M_f and I_f are the foundation mass and moment of inertia, \bar{m} and \bar{M} are the mass density per length of the blade and the tower, v_{bj} and v_{tow} are the absolute velocity of the j^{th} blade and the tower.

The potential energy of the blades can be determined by considering the strain energy of the blades due to bending, centrifugal stiffening and the gravity related potential energy. The potential energy of the blade can be found in (C. Sun 2018a).

Taking the static position of the pendulum as the reference, potential energy of the pendulum can be determined as:

$$V_p = m_p g (L - \sqrt{L^2 - x_r^2 - y_r^2}) \quad (6)$$

Therefore, the total potential energy V of the wind turbine system is:

$$V = V_b + \frac{1}{2} k_t^{fa} q_7^2(t) + \frac{1}{2} k_t^{ss} q_8^2(t) + \frac{1}{2} k_x q_9^2(t) + \frac{1}{2} k_y q_{11}^2(t) + \frac{1}{2} k_{x\varphi} q_{10}^2(t) + \frac{1}{2} k_{y\varphi} q_{12}^2(t) + V_p \quad (7)$$

where V_b is the potential energy of the blades, k_t^{fa} and k_t^{ss} are the fore-aft and side-side stiffness of the tower.

By substituting Eqs. (5) and (7) into Eq. (1), the equations of motion are derived and expressed in a matrix form as:

$$\tilde{M} \ddot{\tilde{q}} + \tilde{C} \dot{\tilde{q}} + \tilde{K} \tilde{q} = \tilde{Q}_{wind} + \tilde{Q}_{uv} + \tilde{Q}_{seismic} + \tilde{F} \quad (8)$$

where \tilde{M} , \tilde{C} and \tilde{K} are the system mass, damping and stiffness matrices. Variables \tilde{Q}_{wind} , \tilde{Q}_{wv} and $\tilde{Q}_{seismic}$ are the generalized force vectors corresponding to wind, wave and seismic loadings.

Details of \tilde{M} , \tilde{C} , \tilde{K} and F can be found in (C. Sun and Jahangiri 2018).

3. Loading

This section presents the derivation of wind, wave and seismic loadings based on the Principal of Virtual Work.

2.1. Wind loading

Wind velocity $v(z, t)$ can be represented by the summation of a constant mean velocity $\bar{v}(z)$ and a turbulent component $\tilde{v}(z, t)$, i.e.,

$$v(z, t) = \bar{v}(z) + \tilde{v}(z, t) \quad (9)$$

In the present study, the logarithmic wind profile is adopted to calculate the mean velocity $\bar{v}(z)$, i.e.,

$$\bar{v}(z) = V_{ref} \frac{\log(z / z_0)}{\log(H_{ref} / z_0)} \quad (10)$$

where V_{ref} is the mean velocity at the reference height $H_{ref} = 90m$. Parameter z_0 is the length of roughness and its value is $z_0 = 0.03$.

The turbulent component of wind velocity $\tilde{v}(t)$ is computed using the IEC Kaimal spectral model which can be expressed as follows:

$$S_v(f) = \frac{4I^2 L_c}{(1 + 6fL_c / \bar{v})^{5/3}} \quad (11)$$

where $S_v(f)$ is the power spectral density function, f is the wind frequency in Hz , I is the wind turbulence intensity and L_c is an integral scale parameter.

To account for the spatial dependency of wind velocity $\tilde{v}(z, t)$ at different points, the cross spectra between two points i and j are defined as:

$$S_{ij}(f) = Coh(i, j; f) \sqrt{S_{ii}(f) S_{jj}(f)} \quad (12)$$

where S_{ij} is the cross spectra, S_{ii} and S_{jj} are the auto spectra at points i and j , respectively. Referring to the IEC spectral mode (B. J. Jonkman and Kilcher 2012), the spatial coherence function is given as:

$$Coh(i, j; f) = \exp \left(-a \sqrt{\left(\frac{fL}{\bar{v}_{hub}} \right)^2 + \left(\frac{0.12L}{L_c} \right)^2} \right) \quad (13)$$

According to the Eqs. (10) to (13), a three-dimensional wind field profile represented by 31×31 velocity grids covering the domain of the rotor disk is generated using the TurbSim program (B. J. Jonkman and Kilcher 2012) where the wind velocity is mapped onto the rotating blades.

In the present study, the Blade Element Momentum (BEM) theory is used to estimate the aerodynamic loading acting on the rotating blades. Time series of the aerodynamic loading are computed based on the momentum theory, the blade characteristics and the operational conditions. The input parameters include the rotor geometry, wind speed and the blade rotational (Hansen 2008).

With reference to (C. Sun 2018a), the normal and tangential forces P_N and P_T acting on each element of the blade can be calculated as:

$$P_N = \frac{1}{2} \rho V_{rel}^2 c C_N, \quad P_T = \frac{1}{2} \rho V_{rel}^2 c C_T \quad (14)$$

where ρ is the air density and c is the chord length; V_{rel} is the relative wind velocity. Parameters C_N and C_T are the normal and the tangential coefficients respectively which can be calculated as: $C_N = \cos \phi C_l + \sin \phi C_d$ and $C_T = \sin \phi C_l - \cos \phi C_d$. The lift and drag coefficients C_l and C_d can be determined from the airfoil data.

By implementing the BEM method, the virtual work δW_{wl} done by external wind load can be determined as:

$$\delta W_{wl} = \sum_{j=1}^3 \left\{ \int_0^R P_{Tj}(r, t) [\phi_{1e} \delta q_j + \delta u_{nac}^{ss} \cos(\psi_j)] dr + \int_0^R P_{Nj}(r, t) [\phi_{1f} \delta q_{j+3} + \delta u_{nac}^{fa}] dr \right\} \quad (15)$$

where $P_{Tj}(r, t)$ and $P_{Nj}(r, t)$ denote the tangential and normal wind loading intensity per unit length on the j^{th} blade. Details on determining the equations of $P_{Tj}(r, t)$ and $P_{Nj}(r, t)$ can be found in (C. Sun and Jahangiri 2018).

In terms of the principles of work and energy, the generalized force Q_j can be determined as:

$$Q_j = \frac{\partial(\delta W_{wl})}{\partial(\delta q_j)} \quad (16)$$

Substituting Eq. (15) into Eq. (16) yields the wind induced generalized forces:

$$\begin{aligned} Q_{j,wind} &= \int_0^R P_{Tj}(r, t) \phi_{1e} dr, \quad Q_{j+3,wind} = \int_0^R P_{Nj}(r, t) \phi_{1f} dr, \quad j = 1, 2, 3 \\ Q_{7,wind} &= \sum_{j=1}^3 \int_0^R P_{Nj}(r, t) dr, \quad Q_{8,wind} = \sum_{j=1}^3 \int_0^R P_{Tj}(r, t) dr \cos(\psi_j) \\ Q_{9,wind} &= Q_{7,wind}, \quad Q_{10,wind} = h Q_{7,wind}, \quad Q_{11,wind} = Q_{8,wind}, \quad Q_{12,wind} = h Q_{8,wind} \end{aligned} \quad (17)$$

More detailed equations on determining the aerodynamic loading can be found in (Sun and Jahangiri 2018).

2.2. Wave loading

Wave loading on circular cylindrical structural members can be estimated using Morison's equation (Faltinsen 1993). The horizontal force dF acting on a strip of length dz can be written as:

$$dF = \frac{\pi D^2}{4} C_M \rho i dz + \frac{\rho}{2} C_D D u |u| dz \quad (18)$$

where C_M and C_D are the mass and drag coefficients which are equal to 1.0 and 1.2 respectively; ρ is water density which is equal to 1025 kg/m^3 , D is the diameter of the tower and the monopile; i and u are the wave induced horizontal acceleration and velocity of fluid particles.

In terms of Ref. (IEC 2009), JONSWAP spectrum is used to generate wave time histories.

Based on the JONSWAP spectrum representation method, the fluid particle velocity u and the acceleration i can be expressed as follows:

$$u = \sum_{j=1}^N \omega_j \sqrt{2S(\omega_j)\Delta\omega} \frac{\cosh[k(z + d_w)]}{T_w \sinh(kd_w)} \sin(\omega_j t - k_j x + \phi_j) \quad (19)$$

$$\dot{u} = \sum_{j=1}^N \omega_j^2 \sqrt{2S(\omega_j)\Delta\omega} \frac{\cosh[k(z + d_w)]}{T_w \sinh(kd_w)} \cos(\omega_j t - k_j x + \phi_j) \quad (20)$$

where k is the wave number, ω is wave frequency, ϕ_j is a random phase angle, d_w is the water depth, T_w is the wave period and z is the vertical ordinate from mean water level.

The surface elevation spectrum determined from JONSWAP spectrum along with the surface elevation time history is illustrated in Fig. 2 (a) and (b). The fluid particle velocity and acceleration time history expressed in Eq. (19) and (20) is illustrated in Fig. 2 (c) and (d).

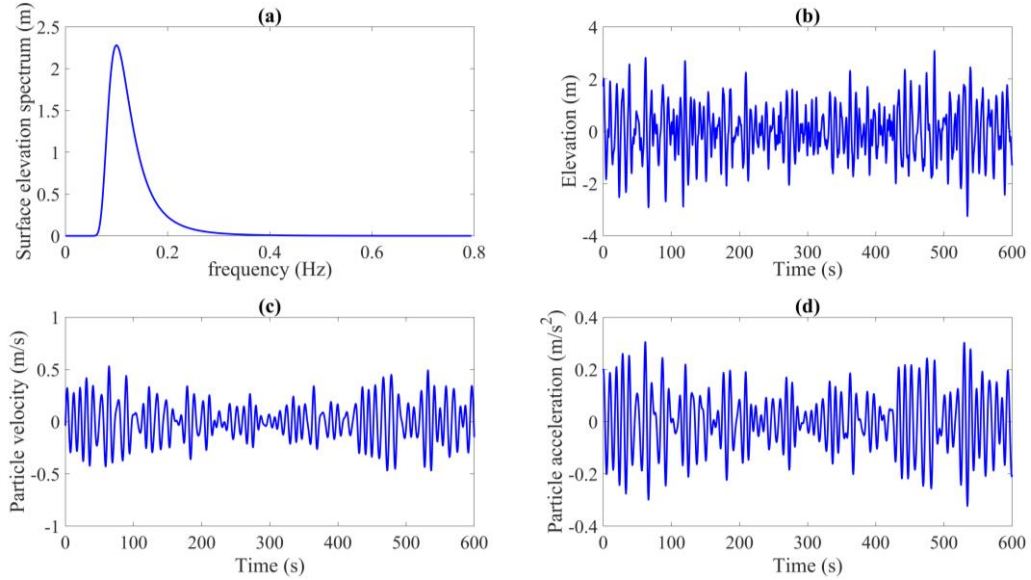


Fig. 2 (a) surface elevation spectrum; (b) surface elevation time history; (c) fluid particle velocity time history at sea water level; (d) fluid particle acceleration time history at sea water level

Virtual work δW_{ww} done by the wave load along virtual displacement δu_{tow} can be written as:

$$\delta W_{ww} = \int_0^\eta dF \delta u_{tow} = \int_0^\eta dF [\phi_{1t} (\cos \beta \delta q_7 + \sin \beta \delta q_8) + \cos \beta (\delta q_9 + z \delta_{10}) + \sin \beta (\delta q_{11} + z \delta q_{12})] \quad (21)$$

Substituting Eq. (21) into Eq. (16) yields the generalized forces corresponding to wave:

$$\begin{aligned} Q_{7,wave} &= \cos \beta F_{wv,1}, & Q_{8,wave} &= \sin \beta F_{wv,1}, & Q_{9,wave} &= \cos \beta F_{wv,2} \\ Q_{10,wave} &= \sin \beta F_{wv,2}, & Q_{11,wave} &= \cos \beta F_{wv,3}, & Q_{12,wave} &= \sin \beta F_{wv,3} \end{aligned} \quad (22)$$

where

$$\begin{aligned} F_{wv,1} &= \int_{-dw}^{\eta(t)} \phi_{1t}(z) dF = \sum_{i=1}^{N_z} \phi_{1t}(z_i) \left[\frac{\rho \pi D^2(z_i)}{4} C_M \ddot{u}(z_i, t) \Delta z + \frac{\rho}{2} C_D D(z_i) \dot{u}(z_i, t) |\dot{u}(z_i, t)| \Delta z \right] \\ F_{wv,2} &= \int_{-dw}^{\eta(t)} dF = \sum_{i=1}^{N_z} \left[\frac{\rho \pi D^2(z_i)}{4} C_M \ddot{u}(z_i, t) \Delta z + \frac{\rho}{2} C_D D(z_i) \dot{u}(z_i, t) |\dot{u}(z_i, t)| \Delta z \right] \\ F_{wv,3} &= \int_{-dw}^{\eta(t)} z dF = \sum_{i=1}^{N_z} z_i \left[\frac{\rho \pi D^2(z_i)}{4} C_M \ddot{u}(z_i, t) \Delta z + \frac{\rho}{2} C_D D(z_i) \dot{u}(z_i, t) |\dot{u}(z_i, t)| \Delta z \right] \end{aligned}$$

2.3. Seismic loading

Let \ddot{u}_{gx} and \ddot{u}_{gy} denote the seismic acceleration components in x and y directions. Consider an infinitesimal unit dr of the blade, the effective earthquake force components acting on dr in x and y directions are $-\bar{m}\ddot{u}_{gx}dr$ and $-\bar{m}\ddot{u}_{gy}dr$. The virtual work $\delta W_{seismic,bl}$ done by seismic loading on the blades can be expressed as:

$$\delta W_{seismic,bl} = \sum_{j=1}^3 \left[\int_0^R -\bar{m}\ddot{u}_{gx}(\phi_{1f}\delta q_{j+3} + \delta u_{nac}^{fa})dr + \int_0^R -\bar{m}\ddot{u}_{gy}(\phi_{1e}\delta q_j \cos \psi_j + \delta u_{nac}^{ss})dr \right] \quad (23)$$

The virtual work done by seismic loading on the nacelle and the tower can be determined similarly:

$$\delta W_{seismic,nac} = -\ddot{u}_{gx}M_{nac}\delta u_{nac}^{fa} - \ddot{u}_{gy}M_{nac}\delta u_{nac}^{ss} \quad (24)$$

$$\delta W_{seismic,tow} = -\int_0^h \ddot{u}_{gx}\bar{M}(\delta q_7\phi_{1tow}^1 + \delta q_9 + \delta q_{10}l)dl - \int_0^h \ddot{u}_{gy}\bar{M}\delta q_8\phi_{1tow}^1dl \quad (25)$$

where M_{nac} denotes the nacelle mass, \bar{M} denotes the mass density of the tower and ϕ_{1tow}^1 denotes the first mode shape of the tower.

The virtual work done by seismic loading on the entire OWT system consists of the virtual work done on the blades, the nacelle and the tower can be obtained as:

$$\delta W_{seismic} = \delta W_{seismic,bl} + \delta W_{seismic,nac} + \delta W_{seismic,tow} \quad (26)$$

Substituting Eq. (26) into Eq. (16) yields the earthquake induced generalized forces:

$$\begin{aligned} Q_{j,seismic} &= -m_{1e} \cos(\psi_j) \ddot{u}_{gy}, & Q_{j+3,seismic} &= -m_{1f} \ddot{u}_{gx}, & j &= 1, 2, 3 \\ Q_{7,seismic} &= -(3m_0 + M_{nac} + M_{1tow}) \ddot{u}_{gx}, & Q_{8,seismic} &= -(m_0 \cos(\psi_j) + M_{nac} + M_{1tow}) \ddot{u}_{gy} \\ Q_{9,seismic} &= -(3m_0 + M_{nac} + M_{0tow}) \ddot{u}_{gx}, & Q_{10,seismic} &= -(3hm_0 + hM_{nac} + M_{2tow}) \ddot{u}_{gx} \\ Q_{11,seismic} &= -(3m_0 + M_{nac} + M_{0tow}) \ddot{u}_{gy}, & Q_{12,seismic} &= -(3hm_0 + hM_{nac} + M_{2tow}) \ddot{u}_{gy} \end{aligned} \quad (27)$$

where

$$M_{0tow} = \int_0^h \bar{M} dl, \quad M_{1tow} = \int_0^h \bar{M} \varphi_{tow}^1 dl, \quad M_{2tow} = \int_0^h \bar{M} l dl$$

4. System Parameters

In this section, the associated parameter values of the baseline offshore wind turbine are presented

In the present study, the NREL 5MW OC3 monopile wind turbine model (J. Jonkman et al. 2009) is used. The parameters are listed in Table. 1.

Table 1 Parameters of the NREL 5-MW baseline wind turbine(J. Jonkman et al. 2009)

Gross properties	Rating	5 MW
	Rotor diameter	126 m
	Hub height	90 m
	Cut-in, rated, cut-out wind speed	3 m/s, 11.4 m/s, 25 m/s
	Cut-in, rated rotor speed	6.9 rpm, 12.1 rpm
Blade	Length	61.5 m
	Mass	17,740 kg
	Second moment of inertia	11,776 kgm ²
	1 st edgewise model natural frequency	1.08 Hz
	1 st flapwise model natural frequency	0.68 Hz
	1 st mode damping ratio	0.48%
Nacelle + hub	Nacelle mass	240,000 kg
	Hub mass	56,780 kg
	Hub diameter	3 m
Tower	Height above ground	87.6 m
	Overall mass	267,650 kg
	1 st fore-aft mode natural frequency	0.324 Hz
	1 st side-side mode natural frequency	0.312 Hz
	1 st fore-aft (side-side) modal damping ratio	1%

5. Results and Discussions

The effectiveness of the 3d-PTMD in controlling the bi-directional vibration of the offshore wind turbine is evaluated in this section. With reference to (IEC 2009), three representative operational wind and wave loading scenarios are summarized in Table 2. It is noted that a near-fault (NF) ground motion recorded at the Sylmar Converter Station (SCS142) of the 1994 Northridge earthquake is adopted. In comparison with regular ground motions, the NF ground motions are characterized by pulse-like excitations with a large peak ground acceleration (PGA), as shown in Fig. 3. It is known

that the effectiveness of a TMD decreases as the duration of the excitation pulse becomes shorter. As a result, the application of a TMD is limited when the primary structure is under short-duration pulse excitations, such as pulses or pulse-like ground motions occurring in the NF areas. Therefore, NF ground motions are used to examine the performance of the PTMD under pulse-like ground motions. As aforementioned, this is lacked in (C. Sun and Jahangiri 2018).

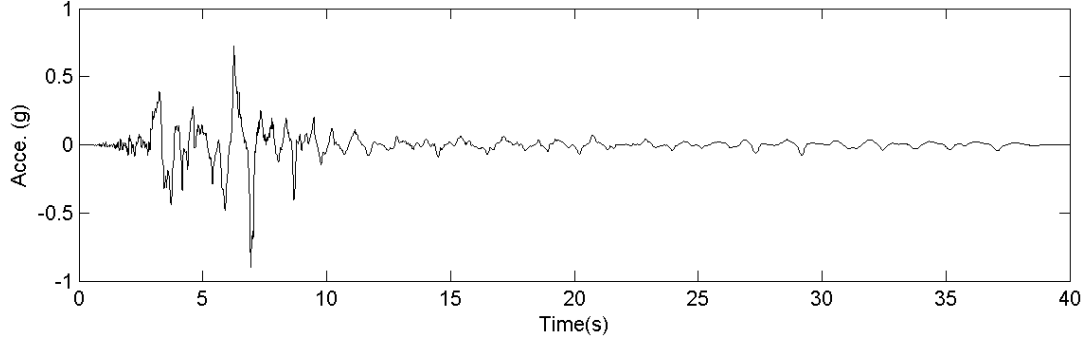


Fig. 3 Recorded near-fault ground motion of 1994 Northridge earthquake at Sylmar Converter Station (SCS142).

Table 2 Load cases considering wind, wave and seismic excitation

Load Case 1(LC1)	Wind speed $v_0 = 12(m/s)$ at hub height, Turbulence intensity $TI = 10\%$ Significant wave height $H_s = 3m$, Wave period $T_p = 10.0s$
Load Case 2(LC2)	Wind turbine parked. 1994 Northridge Sylmar Converter Station (SCS142, $M_w = 6.7$, $PGA = 0.897g$)
Load Case 3(LC3)	Seismic loading + operational wind-wave loading LC1

5.1. Vibration mitigation under misaligned wind-wave loading

Structural responses of the OWT are computed through numerically solving Eq. (8). Fig. 4 (a)–(d) shows the bi-directional motion of the nacelle with and without the 3d-PTMD under the four misalignment wind and wave loading angles. Through comparison, one can clearly observe that the bi-directional response of the nacelle can be significantly mitigated using the 3d-PTMD.

To further evaluate the performance of the 3d-PTMD, the dual TMDs model (referred to as 2TMDs hereafter) studied in Ref. (G. Stewart and Lackner 2013) is adopted for comparison. In terms of Ref. (G. Stewart and Lackner 2013), the optimal frequency and damping ratio are set as: $f_{opt} = 0.94$, $\xi_{opt} = 11\%$ for mass ratio $\mu = 2\%$.

Fig. 5(a)–(d) shows the nacelle bi-directional motion comparison between the 2TMDs and the 3d-PTMD under the four misalignment angles. In Fig. 5(a), the side-side displacement is minimal when wind and wave loading is aligned. It is worth to note that the cross-wind vibration is reported insignificant due to the disturbance of the blade to the wind field and thus is not considered in this paper. In Fig. 5 (b), (c) and (d), it is found that the bi-directional response (fore-aft and side-side) mitigation can be further improved by more than 40% using the 3d-PTMD than the case using the 2TMDs.

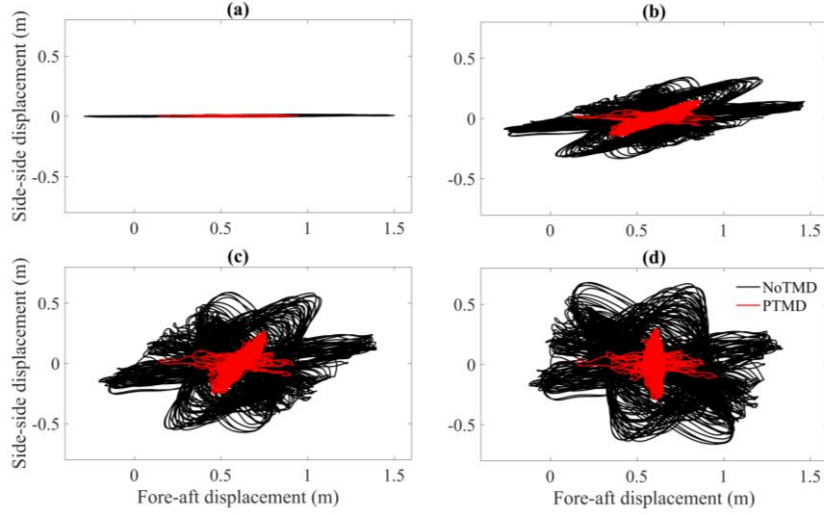


Fig. 4 Nacelle response comparison with and without 3d-PTMD under different wind-wave misalignment (LC1), (a) $\beta = 0^\circ$, (b) $\beta = 30^\circ$, (c) $\beta = 60^\circ$, (d) $\beta = 90^\circ$.

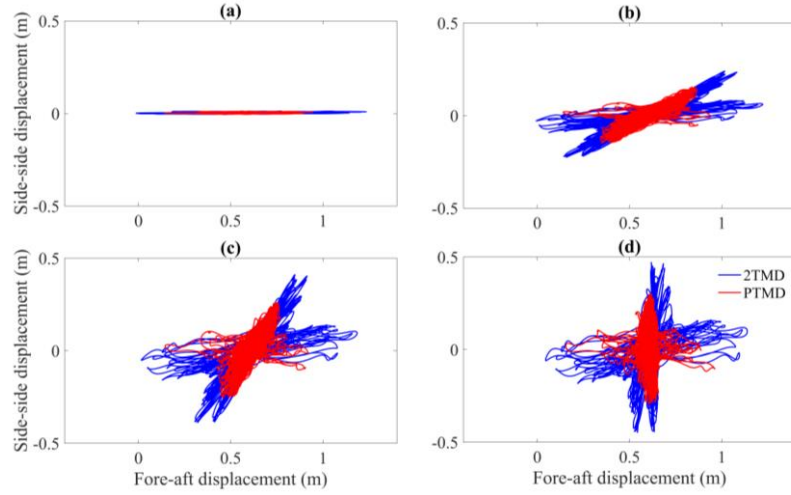


Fig. 5 Nacelle response comparison between linear 2TMD and 3d-PTMD under different wind-wave misalignment (LC1), (a) $\beta = 0^\circ$, (b) $\beta = 30^\circ$, (c) $\beta = 60^\circ$, (d) $\beta = 90^\circ$.

5.2. Vibration mitigation under misaligned wind-wave and seismic loading

The combination of wind and wave loading is more common and critical for monopile OWTs. However, it is probable that an earthquake occurs during the operation of the OWTs in earthquake-prone areas. In the present paper, two scenarios, i.e., the parked condition (LC2) and the operational condition (LC3) are considered. The seismic loading is set to start at $t = 100s$ and end at $t = 140s$. It is noted that different wind-wave and wind earthquake misalignment angles β and β_2 have been

used and similar results were obtained. As a general illustration, the results in the case of $\beta = 30^\circ$ and $\beta_2 = 90^\circ$ under LC3 are presented.

Fig. 6(a) and (b) show the nacelle fore-aft and side-side displacement time-history comparison between the 2TMD and the 3d-PTMD under the combined wind, wave and earthquake loading LC3. It is indicated in Fig. 6(a) and (b) that under near-fault ground motions, the 3d-PTMD can mitigate the pulse excited structural response to a lower level more rapidly than the 2TMD. The reduction effect of the acceleration is presented in Fig. 7 where it is found that the 3d-PTMD outperforms the 2TMD. Through comparing Fig. 7(a) and (b), one can find that the seismic loading induced acceleration is roughly ten times as large as that caused by operational wind and wave loading. In Fig. 7(b), the mitigation of the acceleration RMS can be improved by around 60% using the 3d-PTMD when compared to the dual linear TMDs.

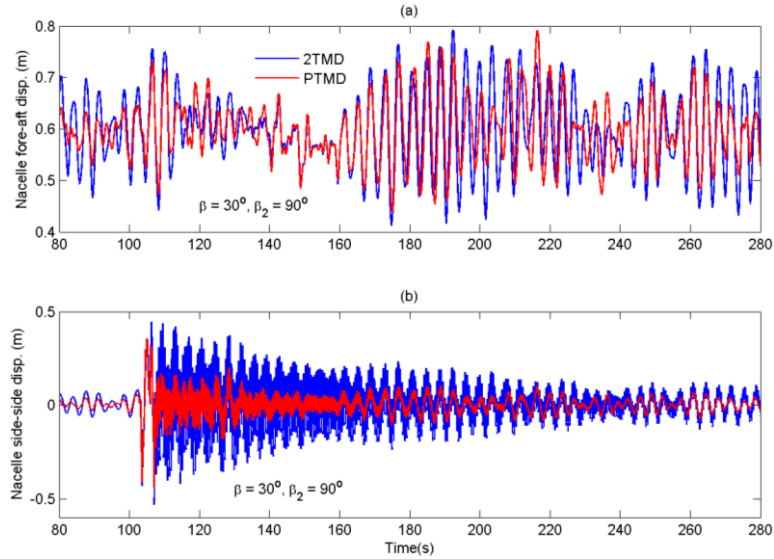


Fig. 6. Nacelle displacement time-history comparison between 2TMD and 3d-PTMD under LC3. The earthquake happens at $t = 100s$ and ends at $t = 140s$.

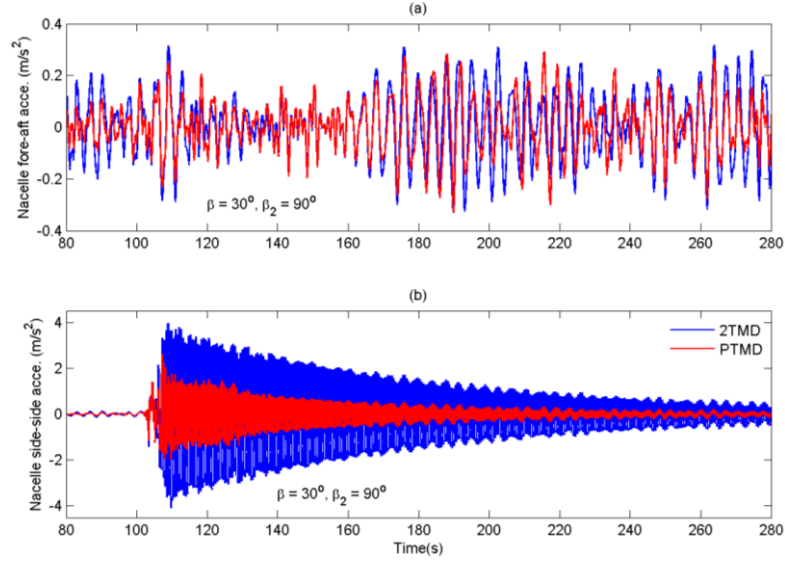


Fig. 7 Nacelle acceleration time-history comparison between 2TMD and 3d-PTMD under LC3. The earthquake happens at $t = 100s$ and ends at $t = 140s$.

5.3. Performance robustness under damage

Due to cyclic environmental loadings acting on the offshore wind turbines, damage can probably occur to the tower and the foundation. To examine the performance robustness of the 3d-PTMD under damage, four damage cases for the foundation and the tower are considered. To model the damage, the foundation and tower stiffness are reduced by 5%, 10%, 15% and 20%.

As a representative case, the time history structural responses under 20% damage for the tower and foundation are presented in Figs. 8 to 11. Figs. 8 and 9 illustrate the nacelle fore-aft and side-side displacement time history comparison between the 3d-PTMD and the 2TMDs in the case of 20% tower damage. It can be observed that the 3d-PTMD outperforms the 2TMDs in the presence of damage.

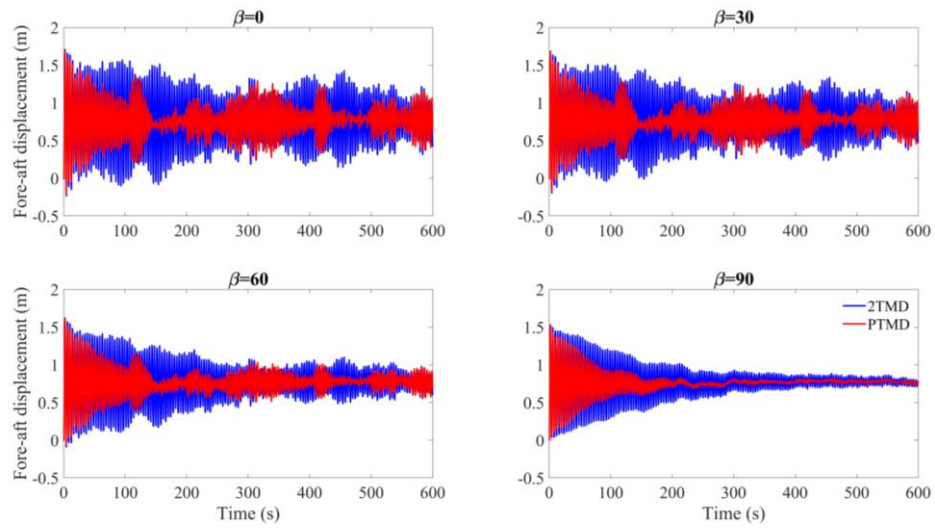


Fig. 8 Nacelle fore-aft displacement reduction comparison between 2TMD and 3d-PTMD under 20% tower damage

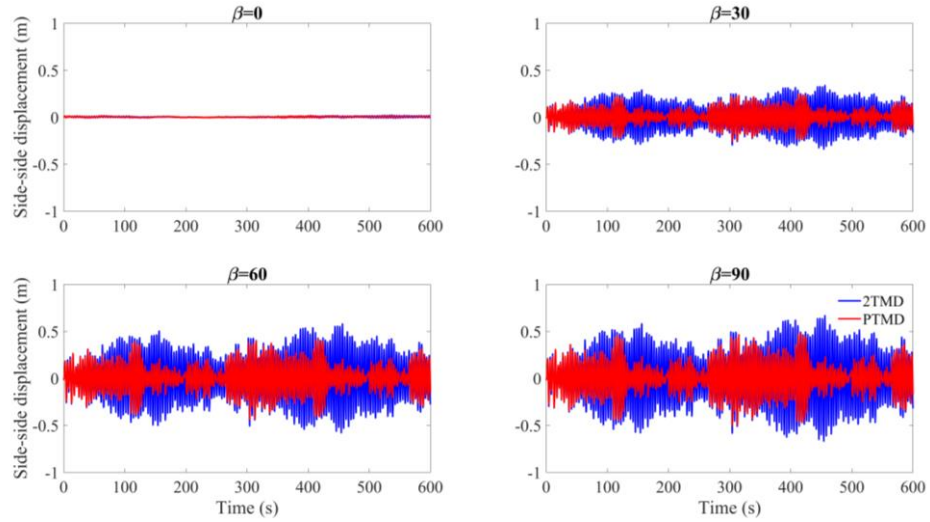


Fig. 9 Nacelle side-side displacement reduction comparison between 2TMD and 3d-PTMD under 20% tower damage

Figs. 10 and 11 show the nacelle fore-aft and side-side displacement time history comparison between the 3d-PTMD and 2TMDs in presence of 20% foundation damage. One can observe that the 3d-PTMD outperforms the 2TMDs under foundation damage. More detailed response comparison results are summarized in Table 3.

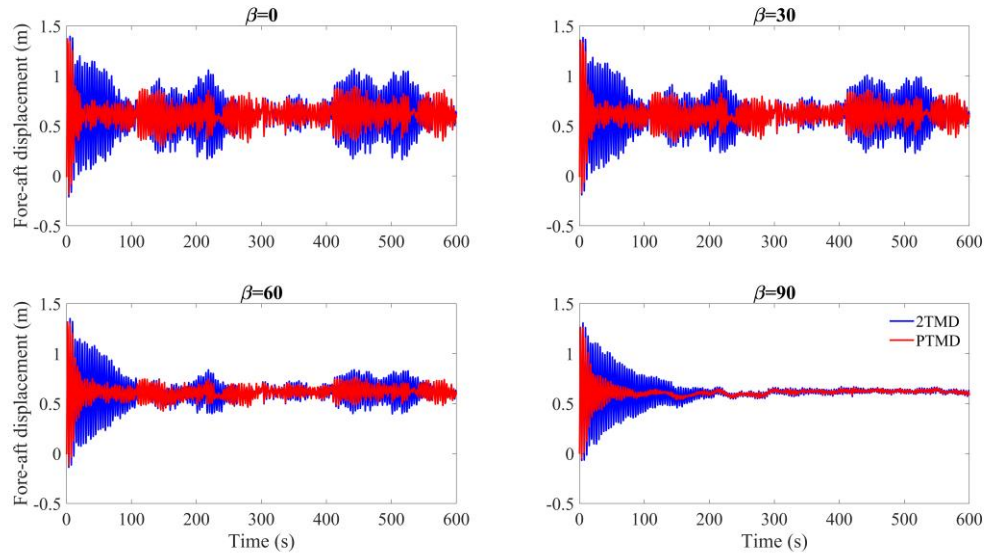


Fig. 10 Nacelle fore-aft displacement reduction comparison between 2TMD and 3d-PTMD under 20% foundation damage

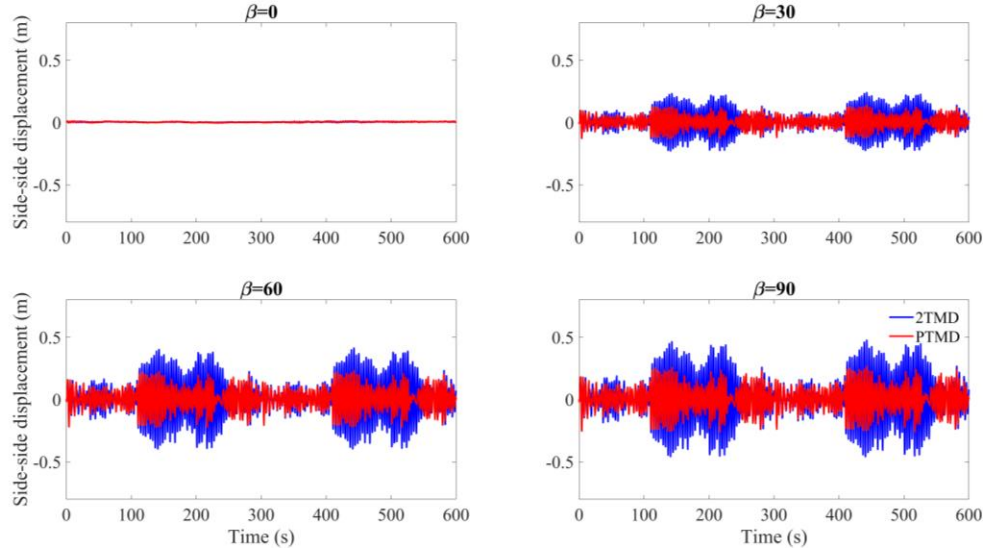


Fig. 11 Nacelle side-side displacement reduction comparison between 2TMD and 3d-PTMD under 20% foundation damage

Table 3 lists the nacelle RMS displacement with different levels of tower and foundation damage from 5% to 20%. It can be found that the 3d-PTMD provides a smaller RMS response for each damage cases, showing that the 3d-PTMD outperforms the 2TMDs in reducing the bi-directional response of the nacelle under tower and foundation damage. It can also be found that the RMS response gradually increases as the damage extent grows. This is due to the fact that by increasing the extent of the damage, the frequency of the primary system continues to vary and the 3d-PTMD and 2TMDs, which are passive tuned mass dampers, become increasingly off-tuned and lose part of their effectiveness. Also, through comparing the results obtained from presence of damage in tower and foundation, it can be found that the tower damage affects the system response more significantly than the foundation damage.

Table 3 RMS response comparison between the 3d-PTMD and 2TMD under different damage cases. Note: the first data corresponds to the RMS response of the nacelle with 3d-PTMD and the second set of data corresponds to the RMS response of the nacelle with 2TMD.

RMS response under tower damage								
β	$D_t = 5\%$		$D_t = 10\%$		$D_t = 15\%$		$D_t = 20\%$	
	FA	SS	FA	SS	FA	SS	FA	SS
0°	0.132, 0.21	0.003, 0.0034	0.146, 0.24	0.003, 0.004	0.187, 0.27	0.004, 0.005	0.237, 0.378	0.004, 0.006
30°	0.121, 0.19	0.051, 0.08	0.135, 0.22	0.058, 0.095	0.171, 0.25	0.07, 0.105	0.221, 0.34	0.081, 0.14
60°	0.093, 0.151	0.091, 0.15	0.101, 0.17	0.11, 0.166	0.133, 0.207	0.128, 0.183	0.171, 0.27	0.149, 0.25
90°	0.075, 0.129	0.101, 0.175	0.088, 0.149	0.11, 0.19	0.11, 0.179	0.152, 0.21	0.14, 0.217	0.172, 0.28

RMS response under foundation damage								
β	$D_s = 5\%$		$D_s = 10\%$		$D_s = 15\%$		$D_s = 20\%$	
	FA	SS	FA	SS	FA	SS	FA	SS
0°	0.12, 0.207	0.0027, 0.0031	0.123, 0.21	0.0027, 0.0031	0.126, 0.21	0.0028, 0.0031	0.129, 0.207	0.0028, 0.0032
30°	0.11, 0.19	0.046, 0.074	0.113, 0.193	0.047, 0.078	0.115, 0.191	0.052, 0.08	0.1173, 0.1885	0.051, 0.088
60°	0.08, 0.15	0.08, 0.128	0.087, 0.15	0.08, 0.136	0.089, 0.147	0.085, 0.145	0.09, 0.145	0.088, 0.152
90°	0.07, 0.112	0.092, 0.148	0.07, 0.115	0.095, 0.157	0.071, 0.12	0.098, 0.167	0.071, 0.121	0.11, 0.176

5.4. Fatigue damage mitigation

The bi-directional tower top displacement causes bi-directional bending moment M_x, M_y in the tower. The resultant stress distribution along the cross-section of the tower becomes complex due to the time-varying relative magnitude of the response in the fore-aft and side-side directions. Because of the symmetry of the cross section, six representative points (referred to as P_1 to P_6) evenly distributed along the out-most semi-circle of the tower cross-section are chosen for fatigue damage estimation. The representative points are illustrated in Fig. 12. The resultant stress of these chosen points are determined as:

$$\sigma_i = \frac{N_x}{A} + \frac{M_x}{I_x} r \sin \varphi_i - \frac{M_y}{I_y} r \cos \varphi_i \quad (28)$$

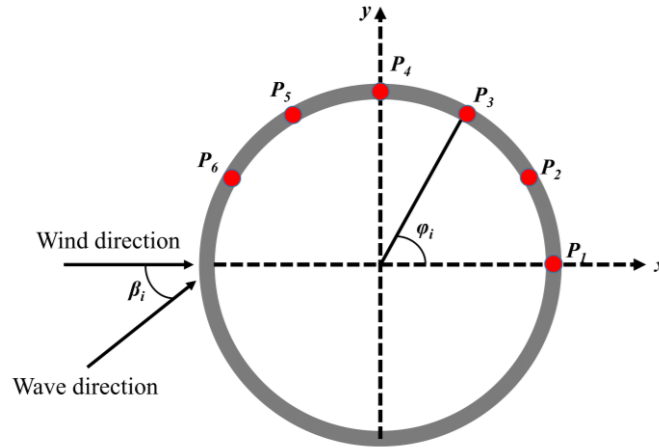


Fig. 12 Representative points distributed along the out-most semi-circle of the tower cross section.

where N_x is the axial force, A is the nominal cross section area, M_x and M_y are the bending moments and I_x and I_y are the sectional moments of area.

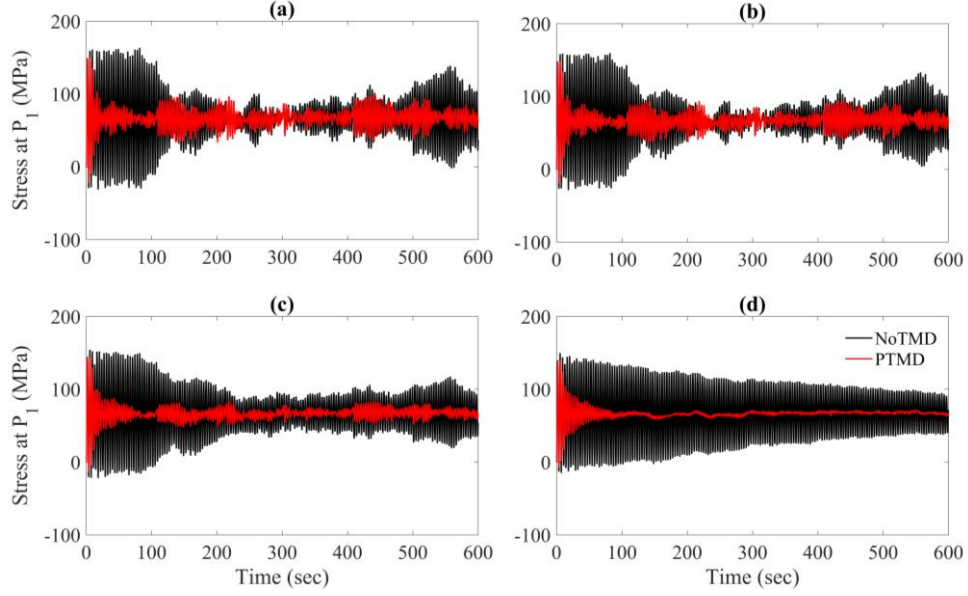


Fig. 13 Comparison of bending stress on foundation-seabed cross section at P_1 with and without 3d-PTMD under different wind-wave misalignment angles (LC1): (a) $\beta = 0^\circ$, (b) $\beta = 30^\circ$, (c) $\beta = 60^\circ$, (d) $\beta = 90^\circ$.

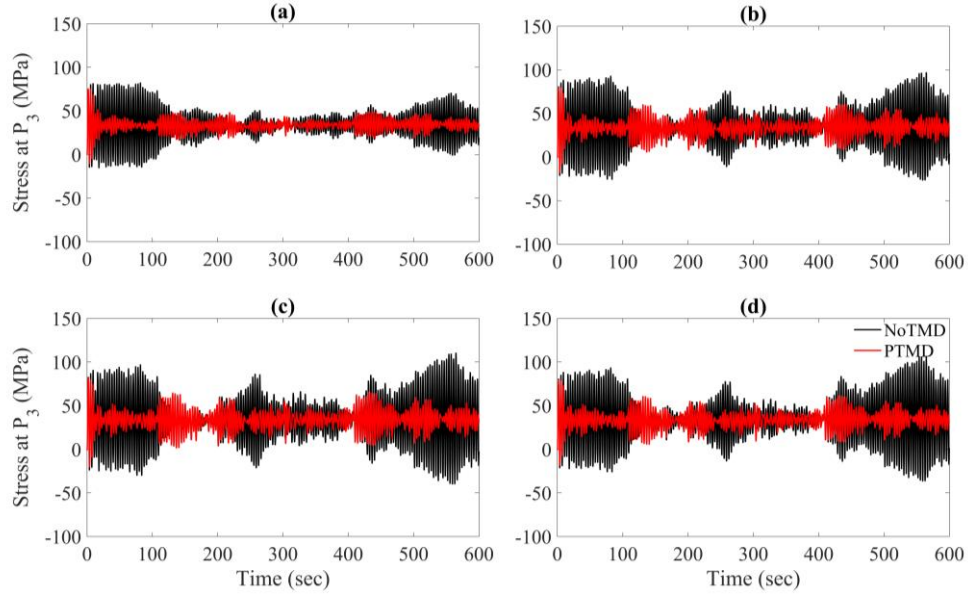


Fig. 14 Comparison of bending stress on foundation-seabed cross section at P_3 with and without 3d-PTMD under different wind-wave misalignment angles (LC1): (a) $\beta = 0^\circ$, (b) $\beta = 30^\circ$, (c) $\beta = 60^\circ$, (d) $\beta = 90^\circ$.

Figs. 13 and 14 (a)-(d) demonstrate the stress time-history at P_1 and P_3 on the foundation-seabed cross section respectively. Through comparison, one can clearly observe that the bending moment stress at both P_1 and P_3 can be significantly mitigated using the 3d-PTMD. Also, it is found that the stress at P_1 is larger than the stress at P_3 .

The rain-flow cycle counting method is applied to calculate the fatigue damage based on the stress time-history of each loading condition. The rain-flow matrix which shows the stress mean, stress amplitude and number of cycles corresponding to wind speed at hub height $v = 12m/s$ and significant wave height $H_s = 3m$ with misalignment angle of 30 degrees for P_1 and P_3 is illustrated in Figs. 15 and 16 (a) corresponding to the controlled wind turbine with 3d-PTMD and (b) corresponding to un-controlled wind turbine point P_1 of foundation-seabed joint.

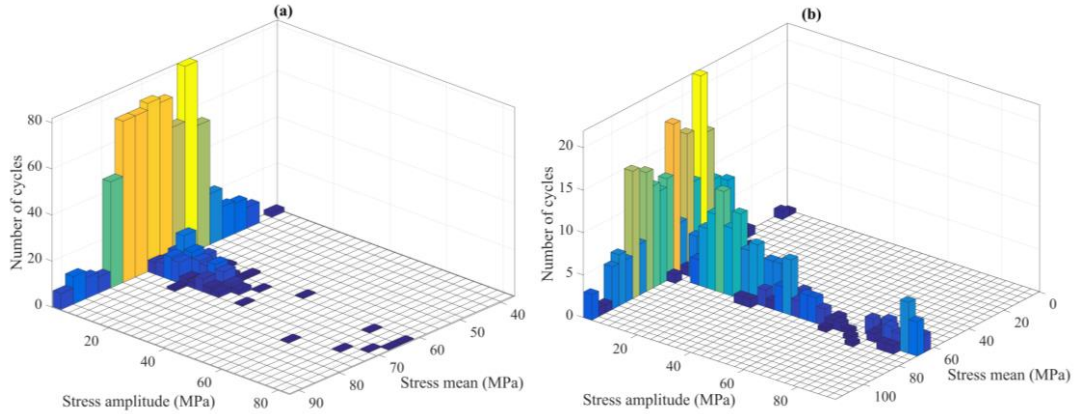


Fig. 15 Rain-flow matrix for P_1 : (a): 3d-PTMD (b): No-TMD.

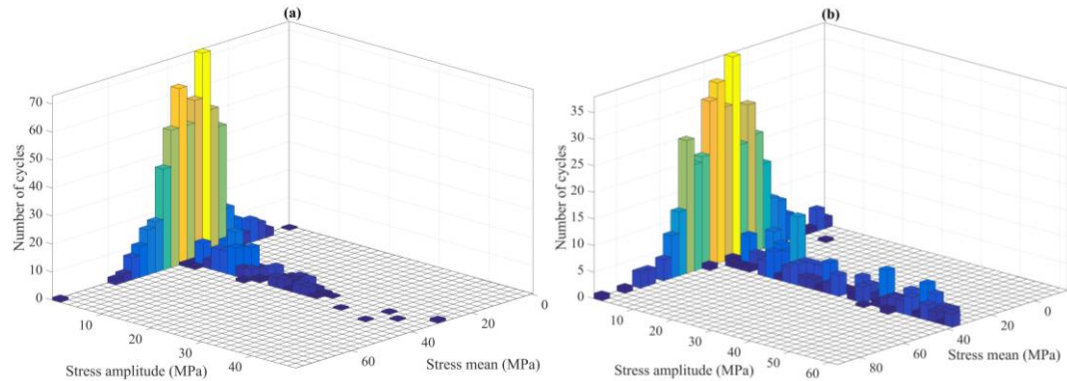


Fig. 16 Rain-flow matrix for P_3 : (a): 3d-PTMD (b): No-TMD

Total fatigue damage is calculated on the basis of the Miner's law expressed as:

$$D = \sum_i^N \frac{n_i}{N_i} \quad (29)$$

where n_i is the number of stress cycles in the i^{th} stress block and N_i is the number of cycles to failure at the design stress range of the i^{th} stress block.

On the basis of the determined number of cycles and stress range, the cumulative fatigue damage of the 6 representative points under wind and wave loading condition is calculated using the S-N curve and Miner's rule. Since the focus of the present study is to evaluate the performance of the 3d-PTMD in mitigating the fatigue damage, the cumulative fatigue damage of each point is determined within 600s rather than a longer window, e.g., 1 hour or 3 hours, to reduce the computational cost.

To demonstrate the effectiveness of the 3d-PTMD, fatigue damage estimation of the tower without control is also conducted for comparison. The final cumulative fatigue damage results of the chosen 6 locations are listed in Table 4. It should be noted that P_{1i} is the representative points distributed along the out-most circle of the foundation-seabed cross section.

Table 4 indicates that on the foundation-seabed cross section, the cumulative fatigue damage within 600s gradually decreases from P_{11} to P_{14} and then gradually increases till P_{16} . In comparison with the No-TMD case, one can find that the 3d-PTMD can increase the mitigation of the fatigue damage by up to 90%.

Table 4 600s cumulative fatigue damage with 3d-PTMD and without control

Location	Location in outer circle	Cumulative fatigue damage (10^{-5})	
		3d-PTMD	No-TMD
Foundation-seabed	P_{11}	2.8569	34.47
	P_{12}	2.6549	30.23
	P_{13}	1.0997	12.09
	P_{14}	0.1511	2.56
	P_{15}	0.197	3.804
	P_{16}	1.3838	18.27

6. Conclusions

In the present paper, a three dimensional pendulum tuned mass damper (3d-PTMD) is used to mitigate the bi-directional vibration of the monopile OWTs under multiple hazards consisting of wind, wave and earthquakes. A fully coupled nonlinear mathematical model of the monopile OWT coupled with the 3d-PTMD is established. The performance of the 3d-PTMD is evaluated and compared with dual linear TMDs. The performance robustness of the 3d-PTMD with damage presence in the foundation and the tower is studied. Using the rain-flow counting method, the fatigue damage mitigation of the tower is also estimated and compared between the case with a 3d-PTMD and that without TMDs. Based on the presented results and discussions, the following conclusions can be obtained:

- When the 3d-PTMD is used, the bi-directional response of the nacelle under different misalignment angles can be mitigated remarkably under all load cases.
- Under near-fault ground motions, the 3d-PTMD responds more rapidly when the pulse-like excitation peak happens and can provide better mitigation of the structural response than the 2TMD.
- In comparison with the 2TMD, the 3d-PTMD with a mass ratio of 2% can improve the mitigation effect of the fore-aft response by more than 45% and the side-side response by more than 40%.
- The short-term cumulative fatigue damage within 600s of the tower can be mitigated by up to 90% when a 3d-PTMD with a mass ratio of 2% is used under operational wind-wave conditions.
- Passive mass dampers will always lose part of their effectiveness when detuning occurs due to system or environmental variations. It is shown that as the damage extent increases, the 3d-PTMD gradually loses its effectiveness. Through comparison, it is found that the 3d-PTMD is more robust than the 2TMD to overcome the detuning effect in the presence of tower and foundation damage.

Acknowledgment

This work was supported by Louisiana State University Start-up Fund (fund number is 127150013), the Faculty Research Grant (fund number is 127159132) and the Innovation in Engineering Research (FIRE) Grant provided by the College of Engineering at Louisiana State University. This work was also supported by the National Natural Science Foundation of China (51679167). The authors are grateful for all the support.

References

- Arrigan, J., Huang, C., Staino, A., Basu, B., and Nagarajaiah, S.(2014), "A Frequency Tracking Semi-Active Algorithm for Control of Edgewise Vibrations in Wind Turbine Blades." , *Smart Struct. Syst.*, **13** (2), 177–201.
- Colwell, S., and Basu, B.(2009), "Tuned Liquid Column Dampers in Offshore Wind Turbines for Structural Control." , *Eng. Struct.*, **31** (2), 358–68.
- Dinh, V.-N., Basu, B., and Nagarajaiah, S.(2016), "Semi - Active Control of Vibrations of Spar Type Floating Offshore Wind Turbines." , *Smart Struct. Syst.*, **18** (4), 683–705.
- Faltinsen, O.M. (Odd M.(1993), *Sea Loads on Ships and Offshore Structures*. Cambridge University Press.
- Fitzgerald, B., Staino, A., and Basu, B.(2018), "Wavelet-Based Individual Blade Pitch Control for Vibration Control of Wind Turbine Blades."
- Hansen, M.O.L.(2008), *Aerodynamics of Wind Turbines*. Earthscan.
- IEC - Part 3: Design Requirements for Offshore Wind Turbines (IEC 61400-3:2009): *METROLOGY AND TESTING CZECH OFFICE FOR STANDARDS: 8590963839257: Amazon.com: Books*(2009), . Geneva, Switzerland.
- Jonkman, B.J., and Kilcher, L.(2012), "TurbSim User's Guide: Version 1.06.00 DRAFT VERSION."
- Jonkman, J., Butterfield, S., Musial, W., and Scott, G.(2009), "Definition of a 5-MW Reference Wind Turbine for Offshore System Development."
- Stewart, G., and Lackner, M.(2013), "Offshore Wind Turbine Load Reduction Employing Optimal Passive Tuned Mass Damping Systems." , *IEEE Trans. Control Syst. Technol.*, **21** (4), 1090–1104.
- Stewart, G.M., and Lackner, M.A.(2014), "The Impact of Passive Tuned Mass Dampers and Wind-wave

- Misalignment on Offshore Wind Turbine Loads.” , *Eng. Struct.*, **73** 54–61.
- Sun, C.(2018a), “Semi-Active Control of Monopile Offshore Wind Turbines under Multi-Hazards.” , *Mech. Syst. Signal Process.*, **99** (January), 285–305.
- Sun, C.(2018b), “Mitigation of Offshore Wind Turbine Responses under Wind and Wave Loading: Considering Soil Effects and Damage.” , *Struct. Control Heal. Monit.*, **25** (3), e2117.
- Sun, C., and Jahangiri, V.(2018), “Bi-Directional Vibration Control of Offshore Wind Turbines Using a 3D Pendulum Tuned Mass Damper.” , *Mech. Syst. Signal Process.*, **105**.
- Sun, C., and Jahangiri, V.(2019), “Fatigue Damage Mitigation of Offshore Wind Turbines under Real Wind and Wave Conditions.” , *Eng. Struct.*, **178** (January), 472–83.
- Sun, C., Nagarajaiah, S., and Dick, A.J.(2014a), “Family of Smart Tuned Mass Dampers with Variable Frequency under Harmonic Excitations and Ground Motions : Closed - Form Evaluation.” , *Smart Struct. Syst.*, **13** (2), 319–41.
- Sun, C., Nagarajaiah, S., and Dick, A.J.(2014b), “Experimental Investigation of Vibration Attenuation Using Nonlinear Tuned Mass Damper and Pendulum Tuned Mass Damper in Parallel.” , *Nonlinear Dyn.*, **78** (4), 2699–2715.
- Zuo, H., Bi, K., and Hao, H.(2017), “Using Multiple Tuned Mass Dampers to Control Offshore Wind Turbine Vibrations under Multiple Hazards.” , *Eng. Struct.*, **141** 303–15.